Study of Cavity Geometry to Improve Optical Quality of Windows in Hypersonic Flow

by

Matthew Schofield

S.B. Aerospace Engineering
Massachusetts Institute of Technology (2022)
Draper Scholar

Submitted to the Department of Aeronautics and Astronautics
in partial fulfillment of the requirements for the degree of

Master of Science in Aerospace Engineering

at the

MASSACHUSETTS INSTITUTE OF TECHNOLOGY

May 2024

© 2024 Matthew Schofield. All rights reserved.

The author hereby grants to MIT and The Charles Stark Draper Laboratory, Inc. a nonexclusive, worldwide, irrevocable, royalty-free license to exercise any and all rights under copyright, including to reproduce, preserve, distribute and publicly display copies of the thesis, or release the thesis under an open-access license.

Authored by:	Matthew Schofield Department of Aeronautics and Astronautics May 10, 2024
Certified by:	Wesley Harris Department of Aeronautics and Astronautics Thesis Supervisor
Certified by:	Arthur Huang The Charles Stark Draper Laboratory Thesis Supervisor
Accepted by:	Jonathan How Chair, Graduate Committee

Study of Cavity Geometry to Improve Optical Quality of Windows in Hypersonic Flow

by

Matthew Schofield

Submitted to the Department of Aeronautics and Astronautics
on May 10, 2024, in partial fulfillment of the
requirements for the degree of
Master of Science in Aerospace Engineering

Abstract

The optical quality of the window-air system of a flight vehicle in hypersonic flow is simulated. The optical distortion of the window-air system is the metric of merit. Within the earth's atmosphere, vehicles at hypersonic speeds may generate viscous and high-temperature thermal boundary layers. These boundary layers induce a non-uniform displacement of temperature, density, and fluid velocity over the window-sensor system leading to a degradation of optical quality of the system. The heat flux into the system is simulated for various geometries (length-to-depth ratios). Computer-simulated flow fields and time-development of different measures of optical quality are produced using US3D. Conjugate heat transfer is used for simulation of solid temperature development, with materials Aluminum-6061 for the vehicle solid (frame) and Sapphire (Al_2O_3) for the window. Optimal window-air system configurations are discussed for a Mach 7 vehicle at 20 km.

Thesis Supervisor: Wesley Harris
Title: Department of Aeronautics and Astronautics

Thesis Supervisor: Arthur Huang
Title: The Charles Stark Draper Laboratory

Acknowledgments

I would like to thank my wife Catherine for her constant support during the writing of this thesis. She has provided strength in times of weakness and joy in times of stress. Her excitement in response to all of my progress has made it easy to endure each of the challenges I faced.

I would also like to thank my supervisors Prof. Wesley Harris and Arthur Huang. Their expert guidance through the research and thesis-writing process has made the finishing of my degree far easier than I could have hoped for. Prof. Harris has made me feel extremely welcome as a graduate student in the Hypersonic Research Lab and has been an excellent example of stewardship and professionalism throughout my time at MIT. Arthur has been a strong driving force behind my research and thesis development. The scope of this thesis would have been much narrower had it not been for his investment and support along the way.

Jeff DeFelice has also been a huge help on anything and everything optics. As an Aerospace Engineering major, I did not have any familiarity with optical physics when I started my Masters; fortunately, Jeff was able to close any comprehensive gaps and offered plenty of resources to assist in my understanding of the material. John Reinert was also very helpful in answering all of the questions I had regarding the Conjugate Heat Transfer plugin he created to US3D. I feel very grateful for every time he walked me through the correct implementation and application of his code, he saved me a lot of time.

Lastly, and most importantly, I want to thank my family. My parents have put in a lot of work to get me to the place I am today and I will never be able to appropriately show them the gratitude I have for their sacrifices. They knew how important it was for me to get good grades in school before I had any idea what grades were; everything I have accomplished thus far in my life is a result of them.

Contents

List of Figures

List of Tables

Chapter 1

Introduction

High temperature profiles set the hypersonic environment apart from its supersonic counterpart due to the significant effect they have on key components, such as material selection, combustion technology, and flow behavior. Air-breathing hypersonic vehicles can encounter temperatures up to 1900K [15] and re-entry vehicles can see temperatures as high as 3000K [22]. Under these conditions, the hypersonic vehicle body undergoes significant levels of heating that requires specifically-made materials that have high thermal conductivity and limits of stability. While ensuring vehicle survival can become difficult, producing a vehicle design that meets mission constraints becomes even more so.

The ability to interact optically with the external environment is one such constraint. Clear optical sensing on a hypersonic vehicle would have utility towards target acquisition, communication, and alternative navigation techniques. High temperatures in the hypersonic regime require sensors to be placed behind glass windows. These windows can encounter non-uniform heating, which would produce a non-uniform temperature profile, which results in non-uniform displacement and potentially severe optical degradation.

The quality of an optical system depends on the spatial propagation of a plane wave from the object it originates from to the imaging plane. Shown in Fig 1-1 is a spherical wave with an example aberrated wavefront. In the figure, the lens produces the aberrations which result in a distorted image point. This thesis focuses on the

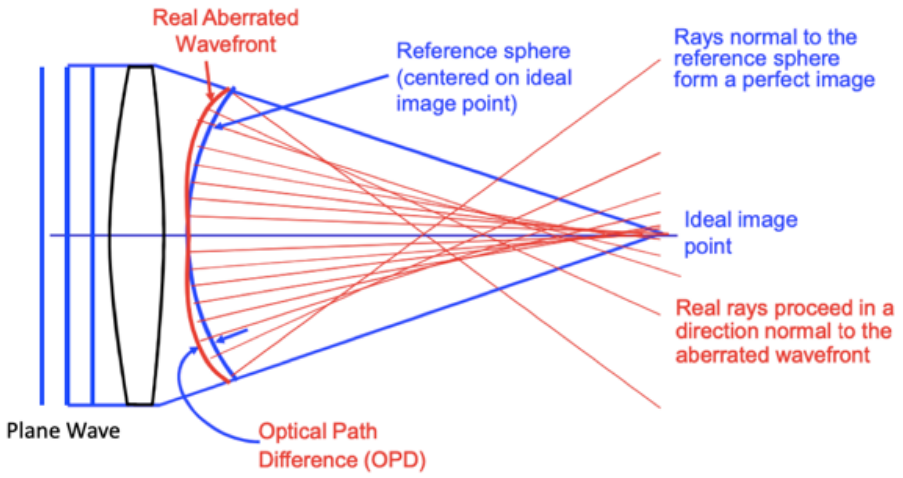

Figure 1-1: Image Error due to Aberrated Wavefront [10]

aberration of the incoming plane wave. This plane wave, also known as a wavefront, can become distorted as different rays within the wavefront shift out of phase, which occurs when rays travel different distances due to varying index of refraction. This thesis considers two sources of index of refraction variation: non-uniform window temperatures and a variation in air density. For the glass window, this is caused by a temperature-dependent index of refraction as well as thermal expansion induced by temperature differentials. For air, the index of refraction has a linear relation to density via the Gladstone-Dale relation [21].

The focus of this thesis is to determine a flow geometry that lengthens the amount of time for which the optical quality of the window-air system remains sufficient. Since the source of this drop in quality is excessive heating rates, the heat-reducing aspect of cavity geometries was chosen for investigation - finite cavities have been shown to diminish floor surface heating by 50-70% [7]; however, cavity geometries aggravate flow behavior by introducing shock waves and inducing turbulence. The presence of unsteady flow causes a variation in fluid density which, as mentioned before, distorts the wavefront. Therefore, this problem is one of optimization: deeper cavities exhibit greater reductions in window heating, but they also introduce greater flow variation.

For the results produced, the only independent variable will be cavity depth. The direct effects of cavity depth will be highlighted by holding the length and width of the

cavity constant, as well as by keeping its location relative to the simulation domain the same. Preserving the free-stream conditions between cases will further isolate these effects. All cases will be run at Mach 7 with inlet flow conditions simulating an altitude of 20km.

For an optical sensor, two things are important: identifying a signal and pinpointing its precise location. The Point Spread Function (PSF), which maps the intensity distribution of a point source on the imaging plane, contains both of these pieces of information. If the peak value of this distribution is not high enough, then the object will be too dark to distinguish against background noise. Additionally, if the location of this peak value is not in the center of the imaging plane, then the vehicle will have difficulty determining the target's real location. Therefore, to understand wavefront distortion, the PSF will be calculated for each geometry as a function of time and will be the basis for deciding which cavity geometry produces the best optical environment.

This thesis will begin by characterizing the problem in Section 2, providing more detail into cavity flow, how it produces optical distortion, and how this optical distortion is measured. Then, in Section 3, the flow environment will be defined, including a description of the flow conditions, the flow geometry, and the materials used for the solid domain. Additionally, the numerical methods implemented for simulating the fluid, the flow of heat from the fluid to the solid, and the temperature-induced displacement of the solid are explained. Finally, in Section 4, the results are analyzed, and in Section 5 conclusions are made on whether or not cavity recession effectively improves the optical quality of windows enduring hypersonic flow conditions.

Chapter 2

Problem Description

2.1 Cavity Flow

This section discusses the fundamentals of cavity flow and the various sources and metrics for optical distortion in a hypersonic flow. Analyzing cavity flow behavior, there are two main categories that cavity geometries fall into: open and closed.

As seen in Fig 2-1, open cavities are too deep for the upstream flow to reattach to the cavity floor. Consequently, the flow upstream of the cavity crashes into the lip of the trailing wall, producing a high level of local heating; fortunately, since the flow does not enter the cavity fully, the velocity, and thus the energy, of the flow inside of the cavity is much lower than it is outside of the cavity. This greatly reduces heating on the cavity floor, which should lessen window deformation. However, circulation of the flow in the cavity may cause substantial aero-optical distortion due to high variations in density.

The main difference present in the closed cavity is cavity-floor reattachment. Since the flow encounters an impingement shock and must bend around the leading cavity edge, the amount of energy entering into the cavity is smaller than it is for the flat plate case. Yet, it does not produces as much of a dampening effect as in the open-cavity case. On the other hand, the variance in density within the cavity should be less than is present in the open cavity due to less flow circulation, making the closed cavity case worth investigating.

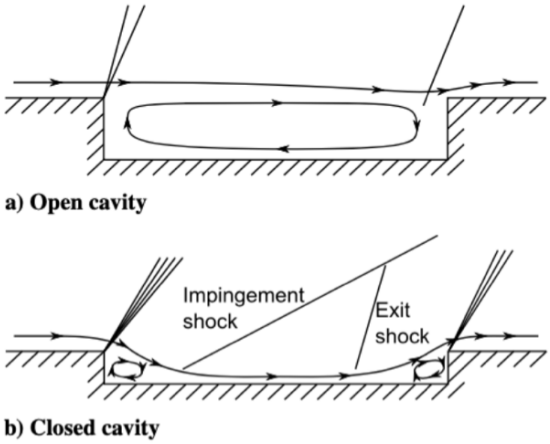

Figure 2-1: Cavity Flow Description [14]

Cavity geometries that have a length-to-depth ratio of $L/D \leq 10$ are considered to be open cavities, while those with $L/D \geq 14$ are closed [14]. L/D ratios that fall between these two numbers are transitional in nature, they oscillate between open and closed flow behavior, and will be ignored for this thesis. The two cavity geometries being considered have $L/D = 2$ (open) and $L/D = 16$ (closed).

2.2 Sources of Optical Distortion

Optical distortion comes from a variation in Optical Path Length (OPL) normal to a given optical plane. The length of distance that light travels, the OPL, is dependent on the index of refraction of the medium through which it is traveling for a given wavelength. Considering the visible spectrum, a vacuum has an index of refraction $n = 1.00$, common air has $n = 1.000293$, and sapphire glass has $n = 1.77$ [19]. For a given physical distance d and constant index of refraction n, $OPL = n * d$ [12]. In a vacuum, the distance light travels is the physical distance, but for other mediums, the distance traveled is longer than the physical distance. Increasing the index of refraction increases the OPL. This becomes important when comparing the distance that two adjacent light waves travel in a medium with varying index of refraction.

In Fig 2-2, two light waves are propagating to the right. The bottom wave encounters glass with an index of refraction of $n = 1.50$. This causes the wavelength to

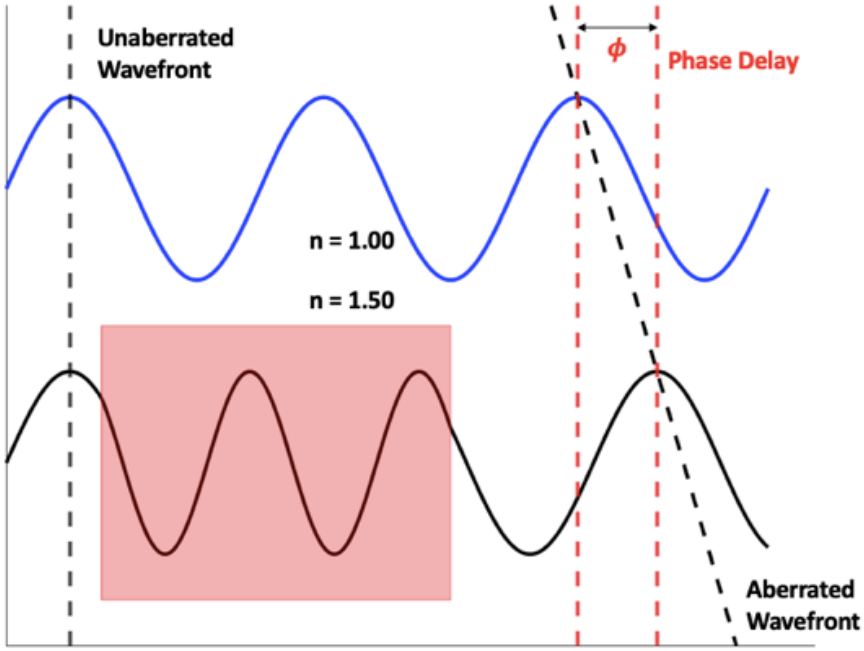

Figure 2-2: Source of Phase Delay

shorten which generates a phase delay once the wave exits the glass. The wavefront, which is the two-dimensional shape produced by matching the locations of equal phase for all light waves, is now distorted. The light waves traveling normal to the glass experience different indices of refraction as they travel through the window-air system. This causes them to all be slightly out of phase, producing an aberrated wavefront. This wavefront is characterized by a two-dimensional array of OPLs. When this array is standardized to have zero mean, it becomes an array of Optical Path Differences (OPDs). The OPD wavefront blurs the image that passes through the system, reducing the amount of information available to the sensor. Additionally, the wavefront may also cause an angular shift, known as boresight error, obscuring the object's real location.

There are two sources of wavefront distortion, both of which add to the two-dimensional wavefront. The air, experiencing a varying density field in space and time, possesses variations in index of refraction. Additionally, the window produces distortions as the index of refraction of glass changes with temperature, as does the thickness of the glass due to thermal expansion.

2.2.1 Aero-Optical Distortion

The Gladstone-Dale equation relates the index of refraction n to the density of air ρ:

$$n = 1 + K_{GD}\rho$$

K_{GD} is the Gladstone-Dale constant [21]. It depends on the medium, the wavelength of light, and the temperature. For this thesis, K_{GD} is assumed equal to $2.26 * 10^{-4} m^3/kg$ [11].

To find the OPL for a single ray of light propagating normal to the glass window, the one-dimensional density array is first translated into one containing index of refraction by the Gladstone-Dale equation. Then, the OPL is calculated via:

$$OPL(x, z) = \sum_i n(\rho_i) * \Delta y(y_i)$$

Where y is the wall-normal direction, Δy is decided by the grid, and the summation is over each element from the window to the edge of the simulation domain. This produces a two-dimensional OPL array which is then standardized into an OPD array by subtracting out the mean.

2.2.2 Window-Induced Distortion

Non-uniform heating of a window results in a non-uniform temperature distribution in the glass. Since the index of refraction of glass depends on temperature and the glass becomes larger due to thermal expansion, a varying temperature distribution produces a medium with varying index of refraction and physical thickness. The OPL for a given coordinate pair can be found using [12]:

$$OPL(x, z) = \sum_i n(T_i) * \Delta y(x, y_i, z)$$

T is the cell-centered temperature and Δy is determined by simulating window displacement via ANSYS Mechanical, an FEA solver. The solver conditions are de-

scribed in Section 3.4. For a wavelength of 3.39μm, the index of refraction of sapphire glass can be found with:

$$n(T) = 1.69927 + 1.139 * 10^{-5}(T - 296)$$

T is the temperature of the glass in Kelvin [24]. This produces a two-dimensional OPL array which can also be made into an OPD array by subtracting out the mean. This OPD array is then added linearly to the OPD array produced via aero-optical distortions to obtain an OPD array that represents the window-air system.

2.3 Measures of Optical Quality

With this two-dimensional OPD array, the optical quality of the window-air system can be measured and analyzed. To measure the impact of the OPD, it must first be translated into phase shift ϕ [1]:

$$\phi = \frac{2\pi}{\lambda} * OPD$$

λ is the wavelength of light; for this thesis, I will be using mid-band infrared light with a wavelength of $\lambda = 3.39\mu$m. Sapphire has high transmission for $\lambda = 3.39\mu$m, 85-86% [6], and a larger wavelength, 3.39μm being near the upper bound for which sapphire demonstrates this high transmission, will reduce the effect of an OPD wavefront by producing a smaller relative phase delay. The equation representing the propagation of light through the window-air system is then [1]:

$$\Psi = e^{i\phi}$$

Ψ is the complex planar wave function which describes the travel of electromagnetic waves through space. To obtain the full expression of the optical wave P, Ψ is then multiplied by a circular pupil function which has value 1 within a circle of radius

R and value 0 outside [4].

$$P = circ(R) * \Psi$$

This replicates the camera device's aperture, which is a circle with radius $R =$ 20mm.

2.3.1 Point Spread Function

As the light from an object propagates to the imaging plane, it diffracts due to edge effects induced by the circular pupil function. Focusing on the diffraction of a point source, rather than of the entire object, allows a closer inspection of the system's optical quality. The diffraction pattern of a point source, known as the Point Spread Function (PSF), can be calculated using [4]:

$$PSF = |\mathfrak{F}\{P\}|^2$$

$\mathfrak{F}\{\}$ being the Fourier Transform. This equation assumes that the light travels sufficiently far before impinging upon the imaging plane, satisfying the Fraunhofer imaging condition [2]. An example is show in Fig 2-3. As can be seen, the light from the object must pass through an aperture of finite width. This causes the incoming plane wave to be cut off on the edges, which induces diffraction. For this thesis, the aperture is a circle rather than a square, and the axis-aligned fringes shown on the imaging plane become radially symmetric rings.

For an unaberrated wavefront, the PSF peaks at the center of the imaging plane and spreads outwards. For a pupil with radial symmetry, the PSF follows a jinc^2 function:

$$\text{jinc}^2(r) = (\frac{J_1(r)}{r})^2$$

$J_1(r)$ is the Bessel function of the first kind and r is the radial distance. The jinc^2 function is depicted in Fig 2-4, alongside a cut of it along the x-axis.

The PSF peaks at the origin and spreads out with radial symmetry. In the presence of optical distortion, the peak might not be at the origin, and it might not be as

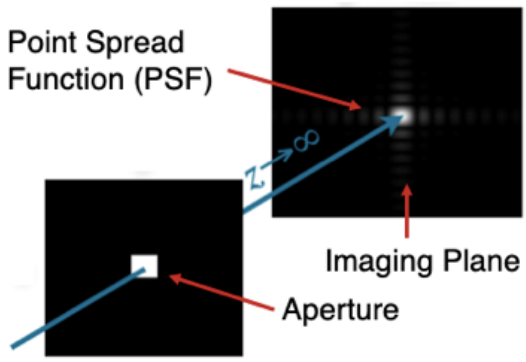

Figure 2-3: Point Source Light Propagation and Diffraction [2]

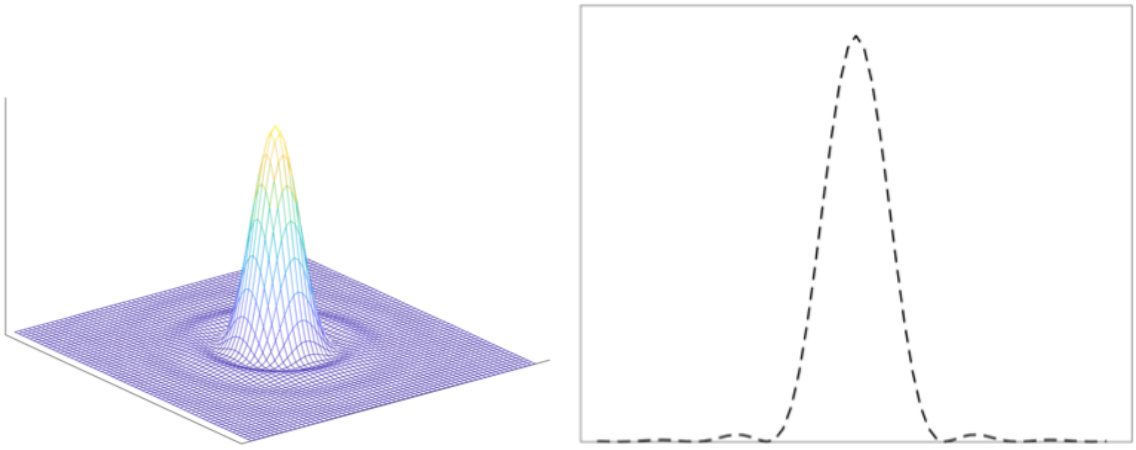

Figure 2-4: Point Spread Function. Left shows the 2D PSF, right shows a 1D slice.

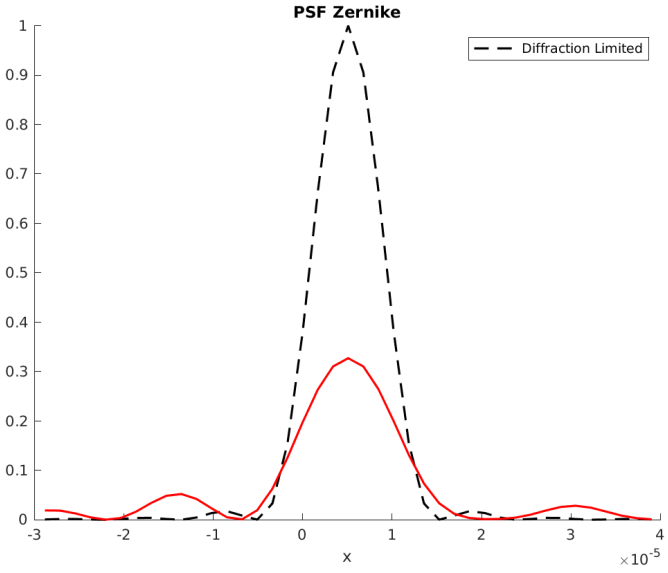

Figure 2-5: Aberrated Wavefront Comparison

high. Fig 2-5 shows the PSF of an aberrated wavefront, compared to one from an unaberrated wavefront. The aberrated wavefront is constructed using Zernike coefficients [18]. The central peak rises to a smaller value than the unaberrated case, demonstrating a loss in intensity. In a practical sense, this would cause a bright spot to appear less bright, reducing the system's ability to distinguish it from noise. The Strehl Ratio (SR) quantifies this loss of intensity due to distortion:

$$SR = \frac{\max(PSF_{aberrated})}{\max(PSF_{unaberrated})}$$

For the Zernike case presented in Fig 2-5, $SR = 0.3270$. The Strehl ratio characterizes the loss of target signal intensity.

2.3.2 Boresight Error

While the Strehl ratio focuses on the value of the PSF at the location where the peak occurs, Boresight Error (BSE) measures the angular shift of the peak of the PSF from

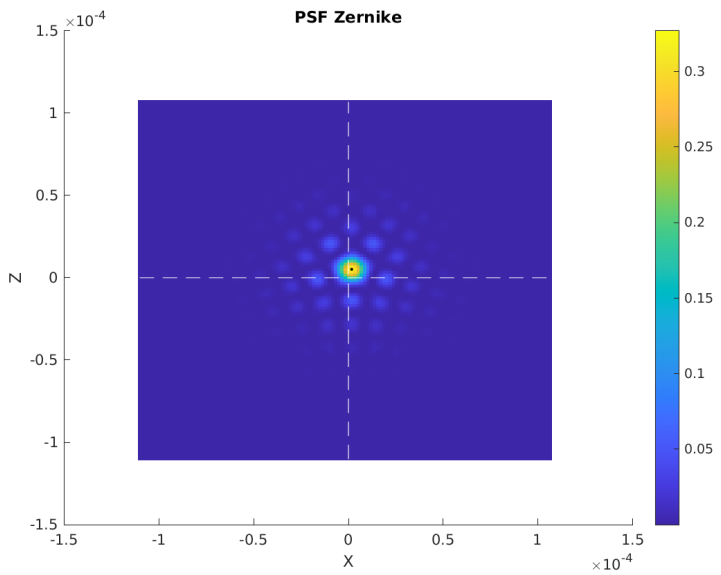

Figure 2-6: 2D Point Spread Function.

the origin. For a given focal length $f = 100m$, the BSE can be calculated via [9]:

$$BSE = tan^{-1}(\frac{\sqrt{x_{peak}^2 + y_{peak}^2}}{f})$$

x_{peak} and y_{peak} are the distances from the peak of the PSF to the origin of the imaging plane. Physical units for x and y on the imaging plane can be found with [8]:

$$x = n_x \frac{\lambda f}{QD}, \quad y = n_y \frac{\lambda f}{QD}$$

$$n_x = n_y = -N/2, -N/2+1, -N/2+2, ...N/2-1$$

λ is the wavelength of light, Q is the aperture padding factor, D is the diameter of the aperture, n_x and n_y are the indices of the array in the x and y directions, respectively, and NxN is the size of the 2D array used to represent the wavefront. Aperture padding is used to increase the resolution of the PSF on the imaging plane. For this thesis, $Q = 2$, $D = 40mm$, and $N = 512$.

Fig 2-6 displays the same PSF from Fig 2-5, but maintaining two-dimensionality. The black dot marks the peak and the white dashed lines mark the axes. The peak

of the PSF has physical shifts of 1.695 μm in the X-direction and 5.085 μm in the Y-direction, producing a BSE of 53.60 μRad. For a target that is directly in front of the sensor, located at the origin of the object plane, the camera sensor will believe that the target is shifted 53.60 μRad away from the origin, causing it to navigate incorrectly. Additionally, since the BSE changes with time due to the flow's unsteady nature, it cannot be accounted for with a pre-set lens adjustment, which can be done in static environments. Ultimately, BSE quantifies the accuracy of the system, given a clear image is produced.

Chapter 3

Flow Environment

This section discusses the flow settings, including inflow conditions, the geometry, and physical properties of the materials used for the solid sections of the flow domain. Additionally, the numerical setup is described, as well as the method used to calculate wavefront results. The flow conditions and geometry chosen are generic and are not tied to a specific use case. Experimental data has not been referenced and will not be used for verification.

3.1 Flow Setup

3.1.1 Free-stream Flow Conditions

All cases are simulated at Mach 7 with air at an altitude of 20km. The altitude is set by a free-stream density of $\rho_\infty = 0.08891 kg/m^3$ and a free-stream flow temperature of $T_\infty = 216.65K$ [13]. This sets the Mach 7 condition with a free-stream velocity of $U_\infty = 2064.76 m/s$. Sutherland's Law is used to calculate the viscosity and, consequently, the Reynolds number. This produces a unit free-stream Reynolds number of $Re_\infty = 8.027 * 10^6 m^{-1}$. All of the walls have an initial temperature of 400K.

3.1.2 Geometry

The window has dimensions of 40mm x 40mm x 5mm in the X, Z, and Y directions, respectively. The three geometries of interest are the flat plate case, the L/D = 2 case, and the L/D = 16 case. Notably, the L/D = 2 case represents an "open cavity", whereas the L/D = 16 case represents a "closed cavity". The flat plate case will be used as a control. Fig 3-1 shows the L/D = 2 geometry. The origin of the coordinate system is the center of the leading edge, where the fluid meets the wall, at the start of the no-slip wall. The domain encapsulates X $\in$ [-0.2m, 0.44m], Y $\in$ [0m, 0.2m], Z $\in$ [-0.12m, 0.12m]. Negative Y values occur only within the cavity, which reaches to -0.02m and -0.0025m for the L/D = 2 and L/D = 16 cases, respectively. The wall boundary condition for negative values of X is a slip wall, which has a length of 0.2m and is not depicted in Fig 3-1. An outflow boundary condition is set at X = 0.44m and a slip wall is used for the boundaries at Y = 0.2m and Z = $\pm$ 0.12m.

For clarity, the inflow condition sets a constant velocity in the X-direction with zero-velocity Y- and Z-components. The no-slip wall enforces zero velocity in all three coordinate directions with zero mass flux through the wall. The slip wall enforces zero velocity in the normal direction with zero mass flux through the wall, requiring the velocity vector to be parallel to the wall surface. The outflow condition does not set any requirements on the flow through the boundary.

In addition to the fluid solver, a conjugate heat transfer solver in the vehicle solid updates the wall temperature over time. The vehicle solid thickness is 0.025m for all cases, which allows for heat to dissipate out of the sides of the window into the body as it would in an experimental scenario. The solid domain is shown in Fig 3-2. More information regarding the conjugate heat transfer solver will be provided in Section 3.3

3.1.3 Materials

Each of the case geometries are simulated with sapphire (Al_2O_3) glass for the window and Aluminum-6061 for the vehicle solid.

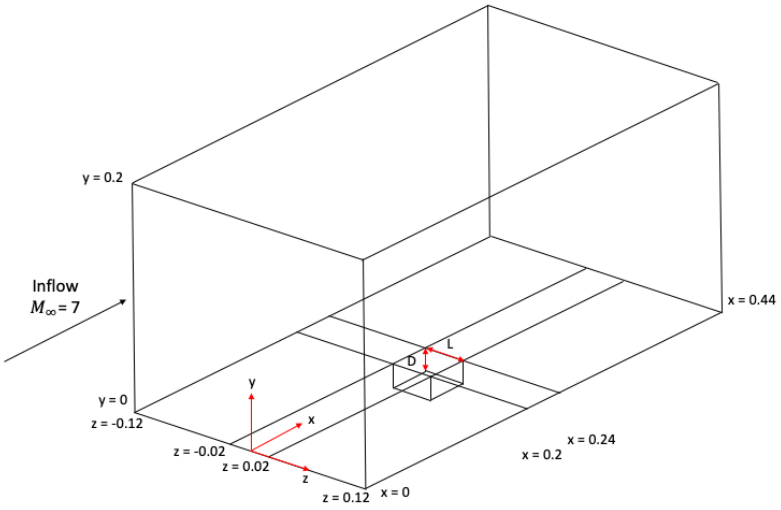

Figure 3-1: L/D = 2 Fluid Grid

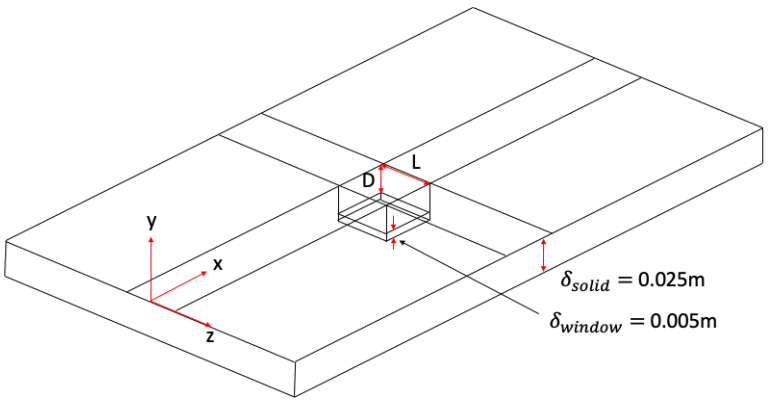

Figure 3-2: L/D = 2 Solid Grid

Temperature	ρ (kg/m^3)	C_p (J/kg-K)	κ (W/m-K)	Emissivity
298K	3970	757.81	119.81	0.5
1273K	3970	1256.05	29.95	0.5

Table 3.1: Sapphire Thermal Properties [16]

Temperature	ρ (kg/m^3)	C_p (J/kg-K)	κ (W/m-K)	Emissivity
0.56K	2700	612.26	87.83	0.91
111K	2700	612.26	83.83	0.91
167K	2700	715.09	111.46	0.91
222K	2700	813.20	131.72	0.91
278K	2700	880.51	147.37	0.91
333K	2700	933.90	161.82	0.91
389K	2700	974.39	180.79	0.91
444K	2700	1009.01	204.81	0.91
500K	2700	1045.93	220.47	0.91
556K	2700	1090.64	229.91	0.91
611K	2700	1144.04	232.36	0.91
667K	2700	1206.63	233.96	0.91
1111K	2700	1206.63	233.96	0.91

Table 3.2: Aluminum-6061 Thermal Properties [17]

Thermal

Table 3.1 shows the thermal properties of sapphire glass, where ρ is the density, C_p is the specific heat, and κ is the thermal conductivity. For all other values of specific heat and thermal conductivity, a linear poly-fit is implemented. Table 3.2 shows the same thermal properties for Aluminum-6061. Poly-fits of order 3 and order 5 are used for intervening values of C_p and κ, respectively.

Mechanical

Table 3.3 shows the mechanical properties used to simulate displacement and thermal stress in the sapphire window. α_{CTE} is the coefficient of thermal expansion and C, for this thesis, is the optical axis (the y-direction). A Young's modulus of 345 GPa and a Poisson's Ratio of 0.29 were used [5].

Temperature	α_{CTE} ($\perp$ to C) (K^{-1})	α_{CTE} ($\parallel$ to C) (K^{-1})
343K	$6.95 * 10^6$	$5.90 * 10^6$
373K	$7.08 * 10^6$	$6.05 * 10^6$
473K	$7.66 * 10^6$	$6.60 * 10^6$
573K	$8.30 * 10^6$	$7.32 * 10^6$
673K	$9.00 * 10^6$	$8.07 * 10^6$
773K	$9.63 * 10^6$	$8.88 * 10^6$
873K	$10.45 * 10^6$	$9.77 * 10^6$

Table 3.3: Sapphire Mechanical Properties [5]

3.2 Numerical Setup

All flow cases are run using the US3D software. It is an implicit finite-volume solver capable of simulating the unsteady three-dimensional form of the Navier Stokes equations. US3D is an upgraded version of the Data-Parallel Line Relaxation (DPLR) code. DPLR combines the high convergence rate of Gauss-Seidel with effective data parallelization, using line relaxation to maintain performance for high-Reynolds number flows [23]. Since DPLR can handle flow discontinuities like shock waves, it is a good fit for the hypersonic flow regime. US3D enhances DPLR by being able to be run on unstructured grids. Additionally, it allows for multiple, independent grids to be simulated together, making methods like conjugate heat transfer, covered in Section 3.3, possible.

Each simulation is run using implicit DPLR time integration with four sub-iterations. A varying CFL number controls the time step. The detached eddy simulation DES97 with SA-Catris is used for turbulence modeling, which switches between RANS and LES depending on cell size. The second-order MUSCL scheme is used for flux extrapolation and modified Steger-Warming flux-vector splitting is used to calculate inviscid fluxes [3].

3.3 Conjugate Heat Transfer

With high temperature fluid profiles, the common isothermal wall assumption cannot be made without significant deviation from a physical solution. In order to accurately

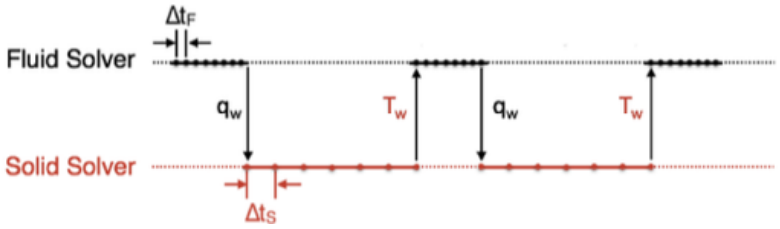

Figure 3-3: Time Marching Algorithm [17]

simulate each flow case, a conjugate heat transfer solver is used to update the temperature of both the vehicle and the window. There are two methods of conjugate heat transfer, one where the fluid and solid are simulated in the same time step, and another where the solver switches between the two. Since the fluid time scale for hypersonic flow is many orders of magnitude smaller than that of the solid, the latter approach must be implemented [17].

For each case geometry, the fluid solver is first run until convergence. From this fluid data, the solid solver extracts the wall heat flux to serve as a Neumann boundary condition for the heat equation that is solved in the vehicle solid. The solid solver simulates the transfer of heat through the domain for a 0.2-second time step, after which the fluid solver runs again until it re-converges. This process continues until the solid has been simulated for 10 seconds. Fig 3-3 shows this time marching behavior.

The solid solver uses the strong form of the heat equation [17]:

$$\rho C \frac{\partial T}{\partial t} = \frac{\partial}{\partial x_i}(k_{ij}\frac{\partial T}{\partial x_{ij}}) + Q \quad \text{on} \quad \Omega_S \times]0, t_s[$$

$$T = \hat{T} \quad \text{on} \quad \Gamma_{S,D} \times]0, t_s[$$

$$-k_{ij}\frac{\partial T}{\partial x_j} n_i = h \quad \text{on} \quad \Gamma_{S,N} \times]0, t_s[$$

$$T(x, 0) = T_0(x) \quad x \in \Omega_S$$

ρ is the density of the solid, C is the specific heat, $T(x,t)$ is the unsteady temperature of the solid, k_{ij} is the thermal conductivity tensor, and n_i is the normal vector on the boundary $\Gamma_{S,N}$. Q is the volumetric heat source, $\hat{T}$ is the boundary temperature, and h is the boundary heat flux [17].

Importantly, the solid domain includes the glass window. By simulating the temperature behavior of the window, appropriate focus can be paid to the thermal stress, and consequent displacement, that the window undergoes.

3.4 Window Displacement

With a three-dimensional array representing the temperature profile in the window, thermally-induced window displacement can be calculated for each point in time. This displacement is caused by temperature differences within the window which cause the glass to expand in a non-uniform manner. This irregular displacement creates optical degradation, which is a motivation for this thesis.

ANSYS Mechanical is used to simulate displacement data based on the thermal behavior of the window for different time-steps. The simulation places a fixed boundary condition on the window, constraining zero displacement on the outer edges of the window. Additionally, the edges are clamped, allowing no rotation.

Fig 3-4 shows an example of the window displacement caused by the thermal behavior inside the window. It depicts the Y displacement on the top and bottom of the window for the L/D = 2 cavity case. Plots 3-4a and 3-4b show the entire domain, with the outermost 9 nodes and 15 nodes removed to better depict the displacement behavior for plots 3-4c and 3-4d and plots 3-4e and 3-4f, respectively. As can be seen, the total amount of displacement that occurs is significant when related to the wavelength $\lambda = 3.39\mu$m. Additionally, the tilted behavior present in the center of the window provides insight into the effect that the window displacement will have on optical distortion.

3.5 Post-Processing

The fluid density and window displacement data are post-processed by scripts written by the author in Python, MATLAB, and Bash. All plotting is produced using MATLAB and the Matplotlib Python library.

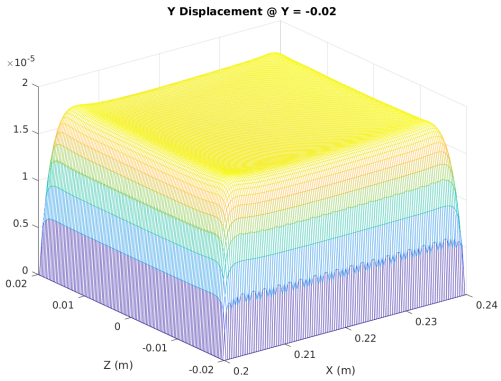

(a) Y Displacement - Window Top

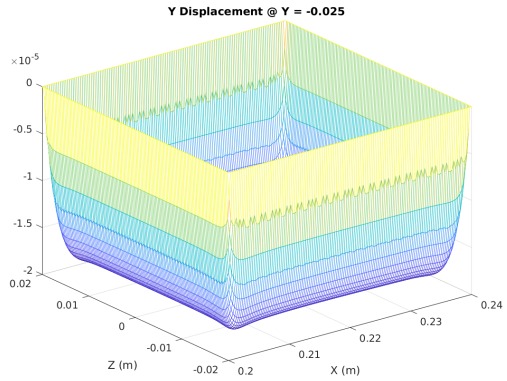

(b) Y Displacement - Window Bottom

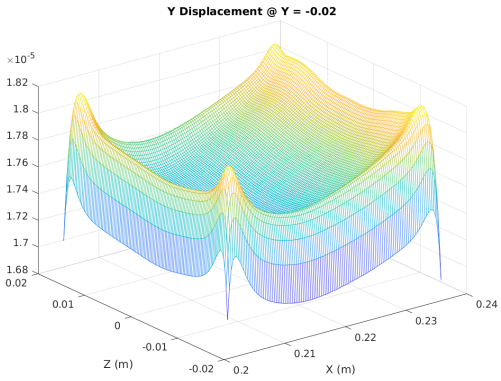

(c) Y Displacement - Window Top

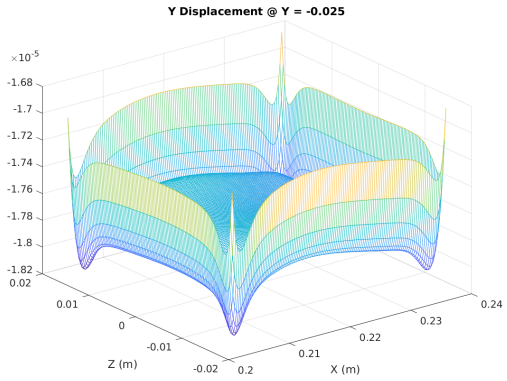

(d) Y Displacement - Window Bottom

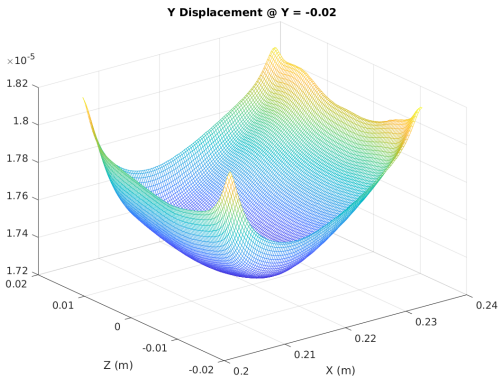

(e) Y Displacement - Window Top

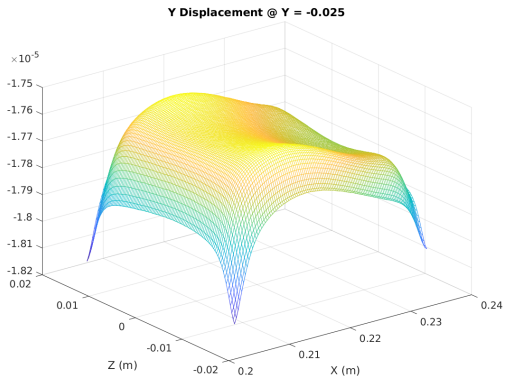

(f) Y Displacement - Window Bottom

Figure 3-4: Window Displacement for L/D = 2

Chapter 4

Results

The optical quality of the window-air system develops with time. To assess optical quality, I will look at the behavior of the PSF, analyzing the time development of SR and BSE. I will also review the temperature development as it pertains to its effect on transmittance through sapphire glass, as well as high-frequency jitter produced by the small time scales present in aero-optical distortion.

4.1 SR Development

Strehl Ratio (SR) is a measure of resolution, as described in Section 2.3.1. The Maréchal criterion states that acceptable image quality is achieved for an SR of 0.80 or higher [10]. The time development of SR for the three geometry cases is provided in Fig 4-1.

As can be seen, all three cases fall short of the Maréchal criterion. Both of the cavity cases show improvement over the flatplate case beyond the 1-second mark, with the L/D = 16 case showing higher optical quality than the L/D = 2 case initially.

Fig 4-2 displays the breakdown of the optical degradation into its two sources. Fig 4-2a shows the aero-optical contribution. The cavity flow cases reduce optical quality, with the relative behavior following intuition - the open cavity L/D = 2 case displays more aero-optical distortion than the closed cavity L/D = 16 case. Notably, the flatplate and L/D = 16 cases do not vary with time. This is to be expected as the

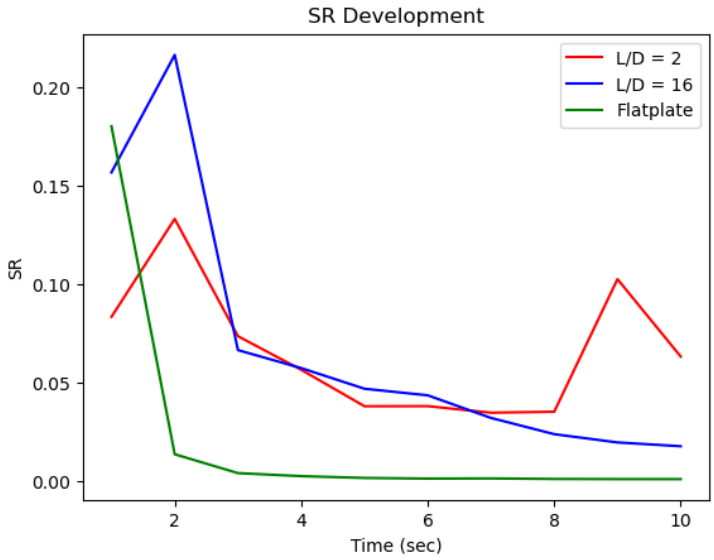

Figure 4-1: Time Development of Strehl Ratio

flatplate case does not show unsteady behavior and closed cavities have been shown to be largely steady, with fluctuations in quantities of interested being less than 0.01% of time-averaged values [14]. In Fig 4-2b, the window-displacement-induced distortions follow closely to what is shown in the combined case in Fig 4-1.

The reason behind the dominant effect that window displacement has over the aero-optics can be understood best by looking at the root-mean-square (RMS) values of the OPD wavefronts. As can be seen in Fig 4-3, the RMS values for the aero-optical distortion are two orders of magnitude smaller than those produced by window displacement. Since these two OPD wavefronts are added to each other, the effects of window displacement outweigh those from aero-optical distortion. This imbalance causes the window-air system to be controlled by the temperature in the window, essentially removing the aerodynamical drawback of cavity recession.

Looking at the values of RMS more closely, those associated with window displacement are on the same order of magnitude of the system's wavelength $\lambda = 3.39\mu$m. This provides insight into why the Strehl Ratio, and consequently the optical quality, of the system is so poor. Further analysis of the wavefront is conducted in Section 4.3.

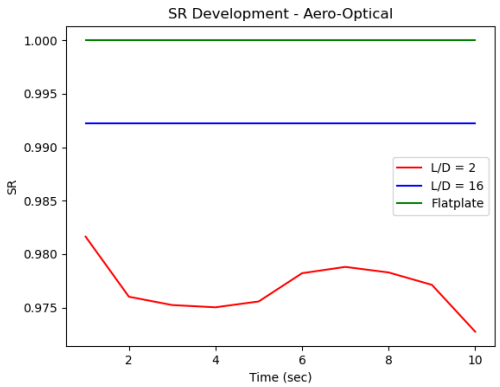

(a) Aero-Optical Contribution

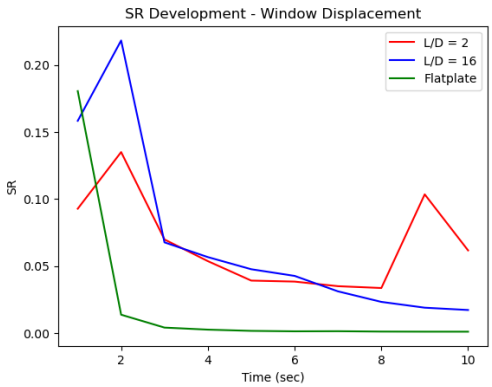

(b) Window Displacement Contribution

Figure 4-2: Strehl Ratio Development Breakdown

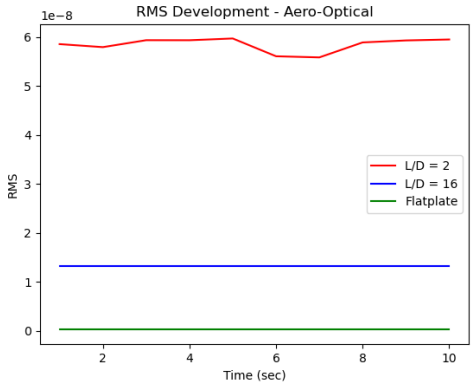

(a) Aero-Optical Contribution

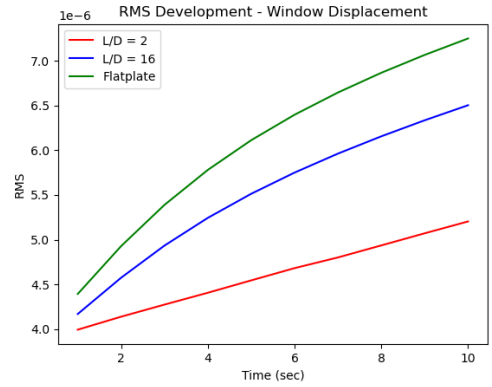

(b) Window Displacement Contribution

Figure 4-3: RMS Development Breakdown

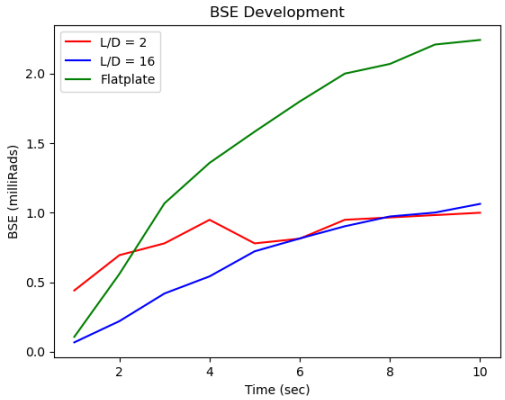

Figure 4-4: BSE of Window-Air System

4.2 Boresight Error

Boresight Error (BSE), as described in Section 2.3.2, is a measure of angular shift. In the context of infrared sensors used for target acquisition, BSE will make it difficult for the system to pinpoint the target's exact location. Since the BSE changes with time, the system cannot account for it as it would in a static environment, making the issue of significant BSE difficult to resolve.

Fig 4-4 shows the BSE development of all three flow geometries. Similar in behavior to the SR development, the first couple of seconds shows the flatplate matching or exceeding the optical quality of the cavity cases, with the L/D = 16 case showing better results than the L/D = 2 case; however, after t = 5.0 seconds, the two cavity cases produce a similar BSE. This result, in connection with the SR development, shows that the L/D = 16 case performs better than the L/D = 2 case for a short time, after which there is little difference.

4.3 Point Spread Function

While single-point metrics such as SR and BSE are helpful in describing the optical quality of the window-air system, direct analysis of the PSF can shed light on the qualitative optical behavior. Analysis will be conducted first on the PSFs for t = 5.0 seconds. Then, since there seems to be unique initial behavior, attention will be

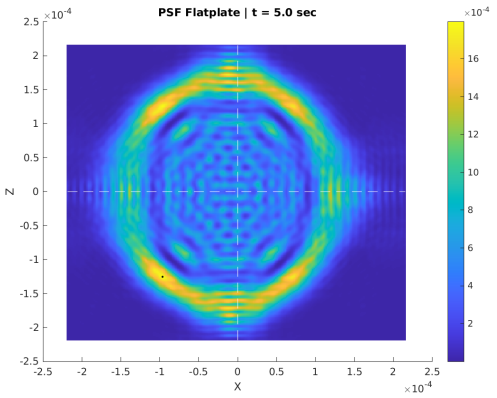

(a) Flatplate @ t = 5.0

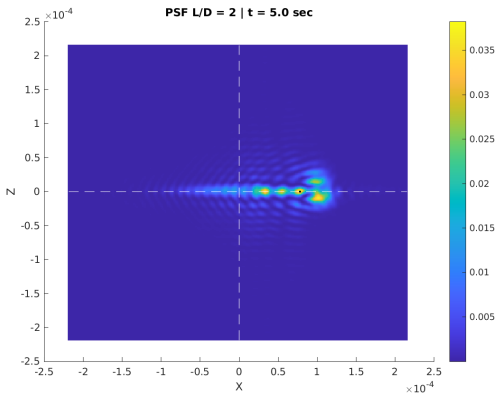

(b) L/D = 2 @ t = 5.0

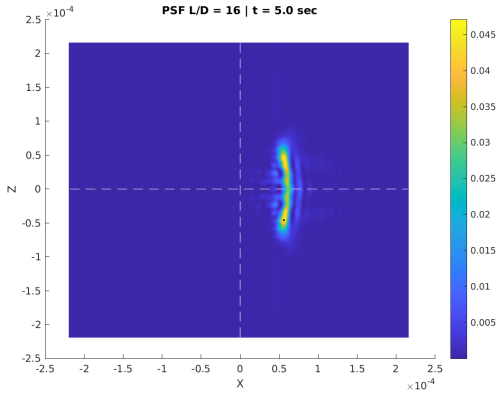

(c) L/D = 16 @ t = 5.0

Figure 4-5: PSF @ t = 5.0 seconds

heeded to the 1.0-3.0 second range, and also at t = 9.0 seconds due to the unexpected peak for L/D = 2 at that point.

4.3.1 t = 5.0 seconds

Fig 4-5 shows the PSF for each of the three flow geometries. From Fig 4-5a, it is clear how poorly the flat plate transfers the location of the object to the imaging plane. The intensity follows a circular pattern, spreading the intensity from the point source onto a large disk. The angular distance to the outer disk from the origin, which is described by the BSE, is 1.583 mRad. This, combined with an SR of 0.0018, paints a blurry picture. The system would have difficulty finding the exact position of the target and, with such a low peak intensity, background noise could make the target's

effect on the imaging plane negligible.

Fig 4-5b and Fig 4-5c show the PSFs from the cavity geometries. For both the L/D = 2 case and the L/D = 16 case, the PSF looks symmetric around the Z-axis. For the L/D = 16 case, the location of peak intensity occurs below the Z-axis, but it is coupled with an almost identical distribution above. The issue for a sensor used in target acquisition is that both of the cavity cases present a multitude of bright sports on the imaging plane. For the L/D = 2 case, there seems to be 4-5 spots that the system could interpret as the location of the target. For the L/D = 16 case, there are 2 peaks, with a longer ride connecting them. To the observer, it seems reasonable that one could construct an algorithm that uses the locations of the bright spots to find the center of mass for the intensity distribution, but this would still produce BSE on the order of 0.5-1 mRad. This would hinder the system's ability to detect the target's location and, as was mentioned for the flatplate case, SR values of 0.0382 and 0.0471 for the L/D = 2 and L/D = 16 cases, respectively, make detection vulnerable to background noise. Notably, though, these SR values are 20-25 times higher than that of the flatplate case.

4.3.2 t ∈ [1.0, 3.0] seconds

Since values for SR at t = 1.0 and t = 2.0 seconds are significantly higher than times afterward, it is useful to analyze them to better understand their development.

Fig 4-6 shows the PSFs for all three geometries at t = 1.0 and t = 2.0 seconds. The same amount of intensity from the point source appears on the imaging plane for each case; thus, distributions that are more spread out necessarily have lower values for SR. For the flatplate case, Fig 4-6a shows the PSF at t = 1.0. The PSF looks far better than it does at 5.0 seconds and better also than at the 2.0-second mark, shown in Fig 4-6b. It has yet to spread out, producing an SR of 0.1805. At t = 2.0, the SR has already dropped to 0.0138, approaching the behavior seen at t = 5.0.

Comparing the two cavity cases, L/D = 2 immediately adopts the pattern present at t = 5.0. The L/D = 16 case, however, maintains a tighter point pattern for both PSFs shown in Fig 4-6e and Fig 4-6f. This accounts for the higher values of SR and

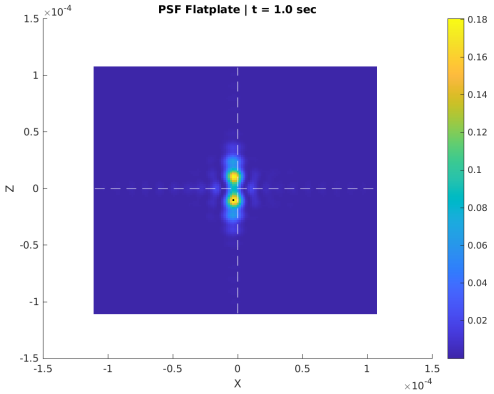

(a) Flatplate @ t = 1.0

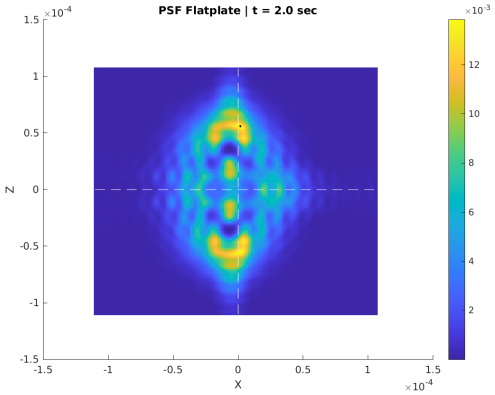

(b) Flatplate @ t = 2.0

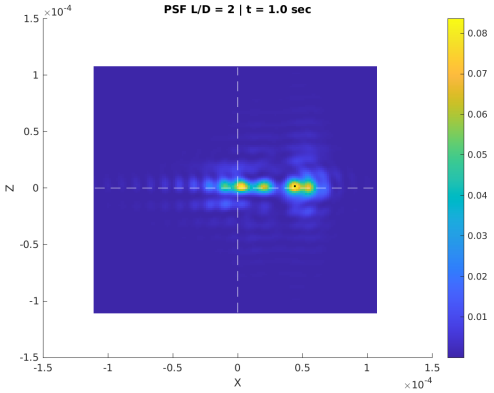

(c) L/D = 2 @ t = 1.0

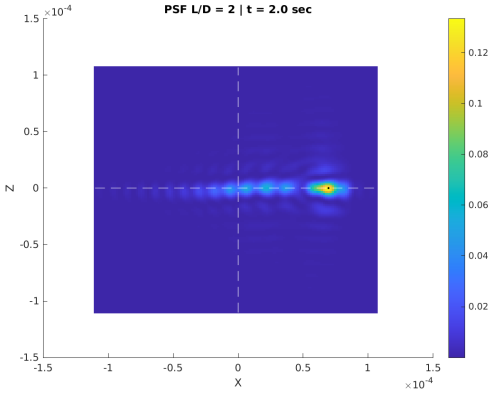

(d) L/D = 2 @ t = 2.0

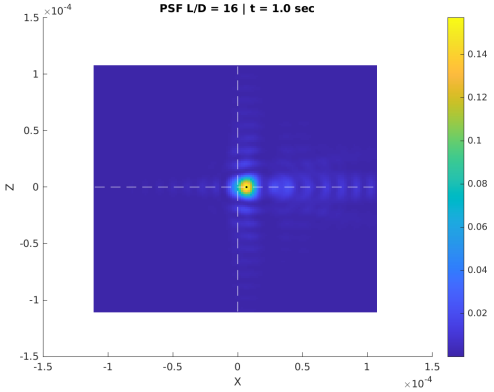

(e) L/D = 16 @ t = 1.0

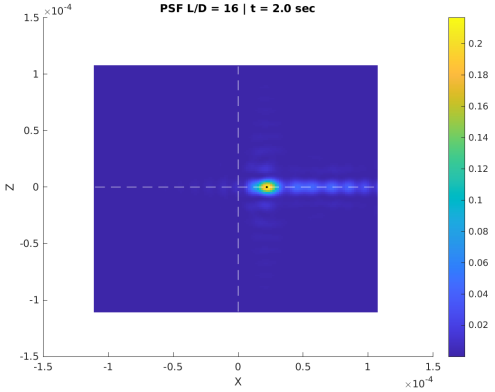

(f) L/D = 16 @ t = 2.0

Figure 4-6: PSF @ t = 1.0 and t = 2.0

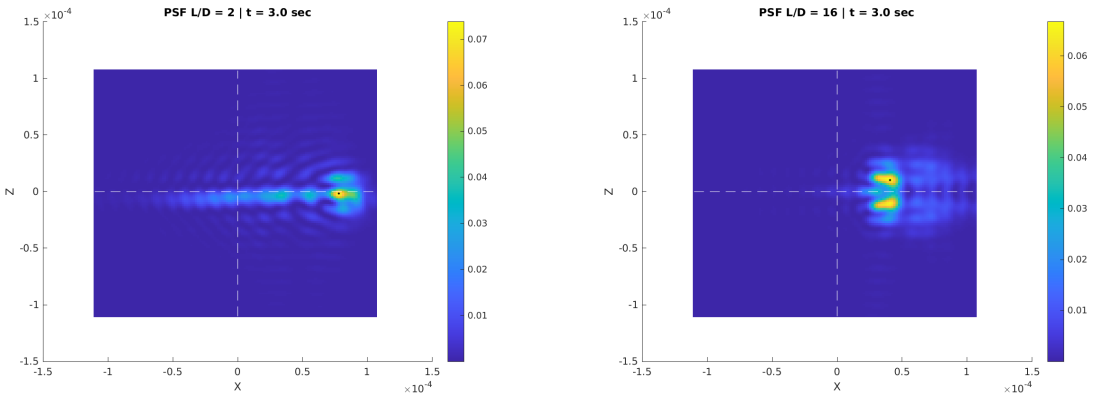

(a) L/D = 2 @ t = 3.0 (b) L/D = 16 @ t = 3.0

Figure 4-7: PSF at t = 3.0

lower values of BSE seen in Fig 4-1 and Fig 4-4. The L/D = 16 pattern at t = 5.0 is not yet seen for these first two time steps, demonstrating why the values of SR for the two cavity cases do not become closer until t = 3.0. Fig 4-7 shows the PSFs of these two cavities at t = 3.0.

Fig 4-7a shows the L/D = 2 case, which follows the behavior seen in all other time steps, namely a cluster of bright spots to the right of the X-axis, on the Z-axis, with a tail trailing to the left. Fig 4-7b shows the L/D = 16 case, illustrating why the SR suddenly drops: the single peak seen in t = 1.0 and t = 2.0 has split into two, adopting behavior more similar to the t = 5.0 case, where the performance of the two cavity cases lines up more closely.

4.3.3 t = 9.0 seconds

Fig 4-1 shows an unexpected jump in SR for L/D = 2 at t = 9.0 seconds.

It seems that, according to Fig 4-8, the collection of bright spots to the right of the X-axis in the L/D = 2 case have consolidated into one, raising the SR. The L/D = 16 case still follows the axis-symmetric behavior seen at t = 5.0. Since the L/D = 2 case is unsteady, the consolidation and breakup of these bright spots will follow a random pattern over time, intermittently producing increases of SR; on the other hand, since the unsteadiness in the L/D = 16 case is negligible, the behavior over

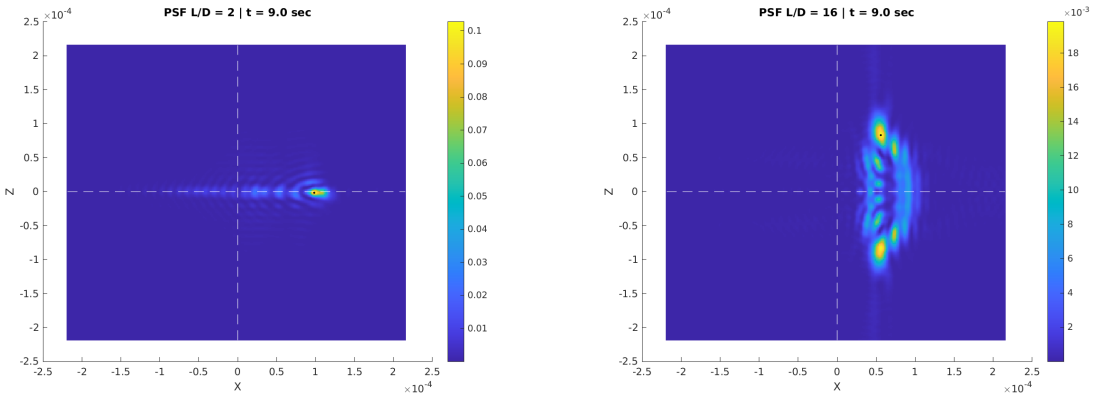

(a) L/D = 2 @ t = 9.0 (b) L/D = 16 @ t = 9.0

Figure 4-8: PSF at t = 9.0

time will follow a more expected development.

4.4 Window Temperature

Since the hypersonic vehicle's optical sensor uses infrared imaging to locate ground targets, the temperature of the glass is a quantity of interest. For high temperatures, a hot window will reduce the window's transmittance, making the image hazy and difficult to recover [20]. Since the basis for this thesis is the reduction of these high temperatures, attention must be paid to the absolute temperature of the window.

Fig 4-9 shows the temperature development of the three geometry cases. The solid line represents the average temperature of the window, and the dashed lines represent the maximum and minimum values. Following intuition, the flatplate case displays the highest temperatures, followed by the L/D = 16 case then the L/D = 2 case.

At t = 10.0, the maximum temperatures are 450K, 476K and 491K for the L/D = 2, L/D = 16 and flatplate cases, respectively. These increases from the initial window temperature of 400K reduce transmission, but analysis must be performed as to understand the extent. Extrapolating from Ref [20], an increase of 91K in the worst case, for $\lambda = 3.39\mu$m could see an increase of as much as 0.05 cm^{-1}. The transmittance τ through the glass, for a non-collimated beam, can be represented by

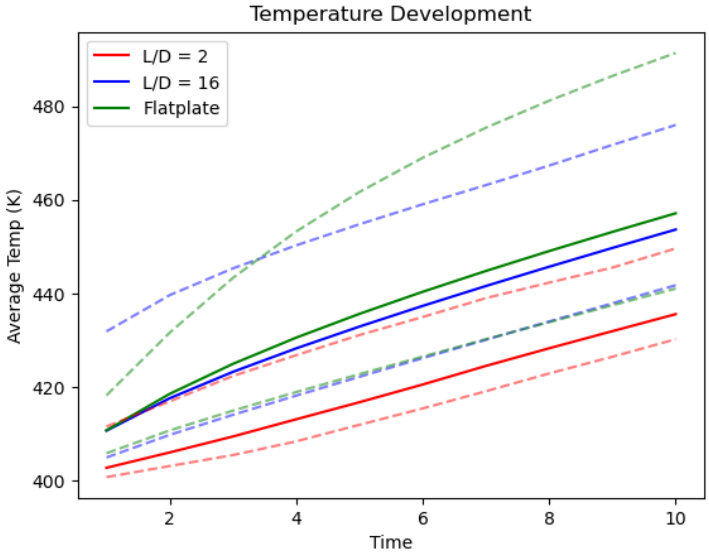

Figure 4-9: Temperature Development

[20]

$$\tau = K^{'}(1-R)^2$$

$K^{'}$ is the bulk attenuation of the material and R is the single surface specular reflectance. $K^{'}$ is related to the extinction coefficient σ via [20]

$$K^{'} = exp(-\sigma L)$$

With $L = 5$mm being the thickness of the material. The extinction coefficient can then be related to the absorption coefficient k with [20]

$$\sigma = k + s$$

s being the scattering coefficient. Using these equations, and assuming the scattering coefficient and single surface specular reflectance are independent of this change in temperature, the change in transmittance τ is related to the change in absorption coefficient via

$$\frac{\tau_{new}}{\tau_{old}} \sim \frac{K'_{new}}{K'_{old}} \sim \frac{exp(-k_{new}L)}{exp(-k_{old}L)} = \frac{exp(-(k_{old}+0.05cm^{-1})L)}{exp(-k_{old}L)} = exp(-0.05cm^{-1}L)_{L=5mm} = 0.975$$

Therefore, using 0.05 cm^{-1} as an upper bound for the change in absorption coefficient would produce a 2.5% decrease in transmittance. In comparison to the optical degradation produced by window displacement, this seems to be negligible and, consequently, should not be a cause for concern at this point.

4.5 Aero-Optical Jitter

One concern with cavity flow is the presence of aero-optical jitter. Since the timescales for cavity flow are so small, $t_{cavity} \sim L/U_\infty \sim 2 * 10^{-5}$ seconds, the PSF produced from aero-optical distortions may move around with high frequency. This high frequency jitter will cause a blurring effect as the timescales for the rest of the system are significantly larger. To produce this jitter effect, the simulation time step was shortened to a constant $dt = 5 * 10^{-9}$. Fig 4-10 shows the BSE of the PSFs produced via aero-optical distortion. All three flow geometries have zero BSE for all time. Due to the presence of the grid, the BSE can only be a range of discrete values. For this case, the smallest perceptible value is BSE= $tan^{-1}(\frac{\lambda}{QD}) = 16.95\,\mu$Rad. If the BSE is smaller than 16.95 μRad, as it seems to be in this case, then a value of 0 is assigned in its place.

Since Gaussian distributions fit well to non-highly-aberrated PSFs [9], the PSF is made continuous by fitting a 2D Gaussian distribution. Fig 4-11 depicts the Gaussian fit to the PSF sliced along the X-axis. The centroid of the Gaussian is non-zero and represents the BSE. For the case shown, the physical shift is -0.4256 μm and 0.0091 μm in the X and Y directions, respectively, producing a radial BSE of 4.2370 μRad. Fig 4-12b shows this calculation performed for each flow case over the same time frame present in Fig 4-10. Consistent with what was shown in Fig 4-2a, the L/D = 16 and flatplate cases are steady and show no variation with time. The L/D = 2

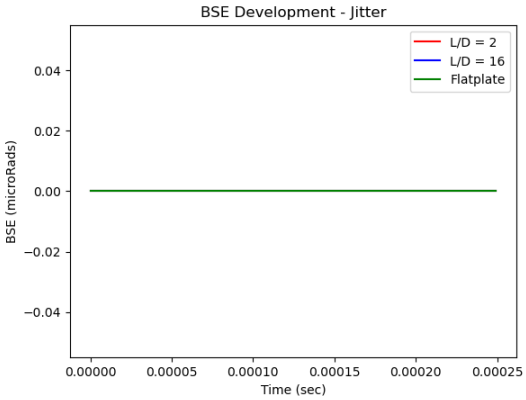

Figure 4-10: BSE for Aero-Optical Jitter - Discrete PSF

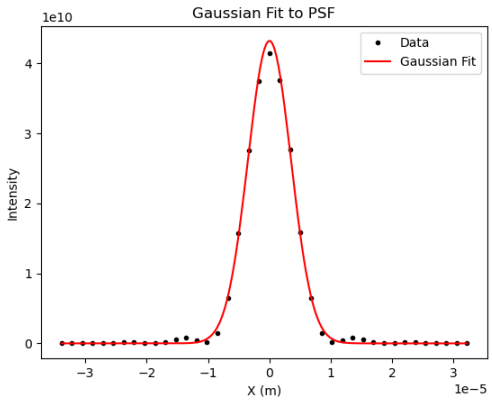

Figure 4-11: Gaussian Fit

case does, displaying BSE values similar in magnitude to that of the L/D = 16 case. Following intuition, both cavity cases show lower values of SR, with the open cavity L/D = 2 case being worse than the closed cavity L/D = 16 case.

To find the blurring induced by aero-optical jitter, the Gaussian fit is first translated onto a more refined grid for each time step. An element-wise average is then performed on these Gaussian distributions, producing a time-averaged continuous PSF. All of the subsequent analysis is performed only for the L/D = 2 case, as the L/D = 16 and flatplate cases are steady.

As can be seen in Fig 4-13, the BSE for the averaged PSF looks to be at the center of mass of the time development distribution. No significant blurring seems to occur as the averaged PSF has an SR of 0.9841, falling within the SR values found in the

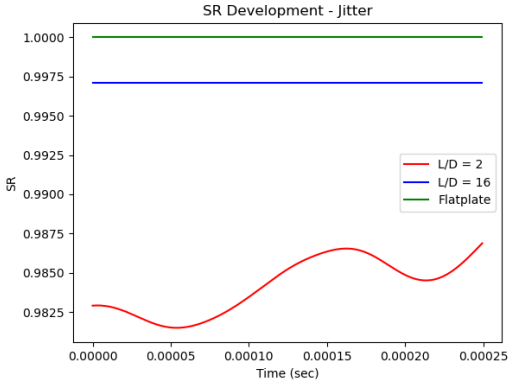

(a) SR Development

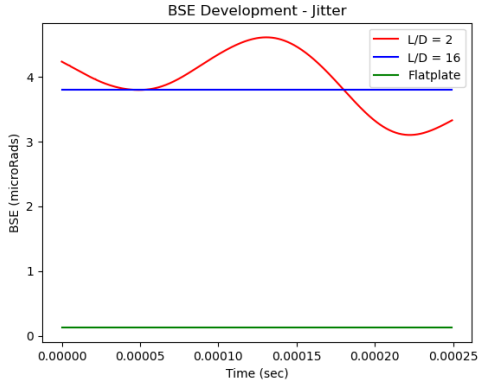

(b) BSE Development

Figure 4-12: Aero-Optical Jitter - Continuous PSF

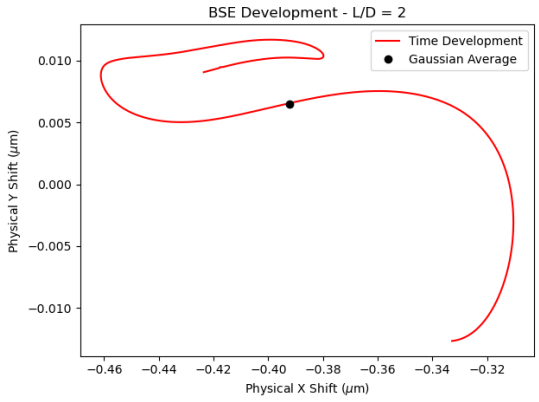

(a) BSE Development vs Average

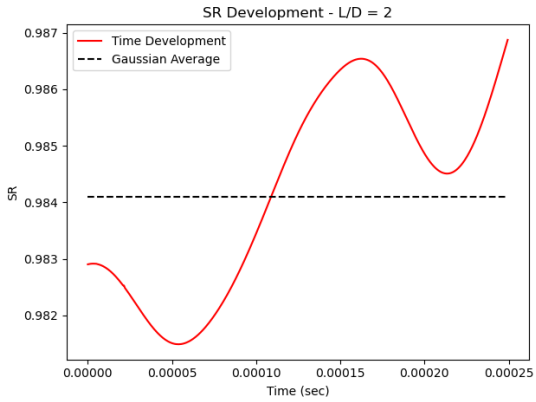

(b) SR Development vs Average

Figure 4-13: Time Development vs PSF Average. The black dot and dashed line in the BSE and SR images, respectively, represent the average, whereas the red lines depict the time development.

time distribution shown in Fig 4-13b. The variation in physical shift, shown in Fig 4-13a, leads to a variation in BSE of [3.1038, 4.6126] μRad. Since the range of BSE values is small, only 1.5088 μRad, the blurring effect induced by the high-frequency jitter of the PSF is negligible, seen by a lack of reduction in SR.

Chapter 5

Conclusion

The goal of this thesis is to analyze to what extent a cavity geometry improves the optical quality of the window-air system on a hypersonic flight vehicle. Based on the results shown in Fig 4-1 and Fig 4-4, as well as the PSFs depicted in Section 4.3, cavity flow does improve optical quality, but not to a level that would prove satisfactory. In Fig 4-1, the SR peaks for each cavity case at t = 2.0 seconds, and only to 0.2167 and 0.1334 for the L/D = 16 and L/D = 2 cases, respectively.

Further analysis, performed in Section 4.3, provides more insight into the optical behavior of all three cases. The main issue with the flatplate case is how spread out the intensity pattern becomes. While the pattern is centered around the origin, any background noise would destroy the system's ability to detect the presence of the object. For the two cavity cases, the intensity pattern is more dense and less susceptible to noise drown out. The main issue for these two cases, though, is that the centers of each pattern demonstrate significant angular displacement. This inaccuracy prevents the sensor from accomplishing its purpose of guiding the missile to successful impact, demonstrating a failure for each of the cavity geometries.

Since this thesis looked only at variation in cavity depth, there is room available for future work to vary other parameters in this problem. This thesis chose an aggressive combination of Mach 7 at an altitude of 20 km. Selecting a higher altitude and lower Mach number would likely lead to better results. Other potential parameters include cavity size, cavity shape, window thickness, and material selection. The main issue

that produced the level of optical distortion present was the magnitude of window displacement relative to wavelength. The geometry that successfully reduces optical degradation will be the one that reduces this window displacement, all other factors are secondary.

Bibliography

[1] George Barbastathis. 3d waves. 2.710 Lecture, 2023.

[2] George Barbastathis. Fresnel and fraunhoffer diffraction. 2.710 Lecture, 2023.

[3] Graham V. Candler, Heath B. Johnson, Ioannis Nompelis, Vladimyr M. Gidzak, Pramod K. Subbareddy, and Michael Barnhardt. *Development of the US3D Code for Advanced Compressible and Reacting Flow Simulations.*

[4] Jeff DeFelice. Aero-optics: OPD wavefront and the point spread function. Unpublished Draper Internal, July 2023.

[5] Valley Design. Properties of sapphire wafers and substrates.

[6] Elena Dobrovinskaya, Leonid Lytvynov, and Valerian Pishchik. *Properties of Sapphire*, pages 55–176. 01 1970.

[7] Joel Everhart, Karen Berger, Ronald Merski, William Wood, Kevin Hollingsworth, Andrew Hyatt, and Ramadas Prabhu. Aero-heating of shallow cavities in hypersonic freestream flow. *NASA Technical Memorandum*, 216846, 2010.

[8] Jack. Wavefront to psf to mtf: Physical units, Feb 2024.

[9] Stuart A. Jackson and Raymond M. Sova. Imaging system aberrations through optical windows with nonuniform laser heating. *Appl. Opt.*, 62(14):3753–3763, May 2023.

[10] Richard Juergens. Opti 517 image quality, 2016.

[11] Wolfgang Merzkirch. *Flow Visualization.* Elsevier, Amsterdam, 1974.

[12] Nathan E. Miller, Daniel Guildenbecher, and Kyle P. Lynch. *Aero-Optical Distortions of Turbulent Boundary Layers: DNS up to Mach 8.*

[13] Data Center National, Geophysical. U.S. standard atmosphere (1976). , 40(4):553–554, April 1992.

[14] Yuya Ohmichi and Kojiro Suzuki. Flow structures and heating augmentation around finite-width cavity in hypersonic flow. *AIAA Journal*, 52(8):1624–1631, 2014.

[15] Robert Quinn and Leslie Gong. Real-time aerodynamic heating and surface temperature calculations for hypersonic flight simulation. *NASA Technical Memorandum*, 4222, 1990.

[16] Rayotek. Sapphire properties data sheet.

[17] John D. Reinert, Anubhav Dwivedi, and Graham V. Candler. *Verification of a conjugate heat transfer tool with US3D.*

[18] Jason Schmidt. *Numerical Simulation of Optical Wave Propagation with Examples in MATLAB*, pages 65–86. 2010.

[19] Anton Skorucak.

[20] Michael E. Thomas, Richard I. Joseph, and William J. Tropf. Infrared transmission properties of sapphire, spinel, yttria, and alon as a function of temperature and frequency. *Appl. Opt.*, 27(2):239–245, Jan 1988.

[21] William Tropf, Michael Thomas, Terry Harris, and Steven Lutz. Performance of optical sensors in hypersonic flight. *John Hopkins APL Technical Digest*, 8(4), 1986.

[22] Michael Winter and Georg Herdrich. *Spectroscopic Observation of the STARDUST Re-Entry in the Near UV.*

[23] Michael J. Wright, Graham V. Candler, and Deepak Bose. Data-parallel line relaxation method for the navier-stokes equations. *AIAA Journal*, 36(9):1603–1609, Sep 1998.

[24] Di Yang, Michael E. Thomas, and William J. Tropf. Infrared refractive index of sapphire as a function of temperature. In Randal W. Tustison, editor, *Window and Dome Technologies and Materials VI*, volume 3705, pages 60 – 69. International Society for Optics and Photonics, SPIE, 1999.